Soft Matter

Pinning-depinning transition of droplets on inclined substrates with a three-dimensional topographical defect

Journal:	*Soft Matter*
Manuscript ID	SM-ART-01-2024-000081.R1
Article Type:	Paper
Date Submitted by the Author:	18-Mar-2024
Complete List of Authors:	Mhatre, Ninad; University of Minnesota, Chemical Engineering and Materials Science Kumar, Satish; University of Minnesota, Chemical Engineering and Materials Science

Pinning-depinning transition of droplets on inclined substrates with a three-dimensional topographical defect

Ninad V. Mhatre and Satish Kumar
Department of Chemical Engineering and Materials Science, University of Minnesota,
Minneapolis, MN 55455, USA

Abstract

Droplets on inclined substrates can depin and slide freely above a critical substrate inclination angle. Pinning can be caused by topographical defects on the substrate, and understanding the influence of defect geometry on the pinning-depinning transition is important for diverse applications such as fog harvesting, droplet-based microfluidic devices, self-cleaning surfaces, and inkjet printing. Here, we develop a lubrication-theory-based model to investigate the motion of droplets on inclined substrates with a single three-dimensional Gaussian-shaped defect that can be in the form of a bump or a dent. A precursor-film/disjoining-pressure approach is used to capture contact-line motion, and a nonlinear evolution equation is derived which describes droplet thickness as a function of the position along the substrate and time. The evolution equation is solved numerically using an alternating direction implicit finite-difference scheme to study how the defect geometry influences the critical inclination angle and the shape of a pinned droplet. It is found that the critical substrate inclination angle increases as the defect becomes taller/deeper or wider along the direction lateral to the droplet-sliding direction. However, the critical inclination angle decreases as the defect becomes wider along the sliding direction. Below the critical inclination angle, the advancing contact line of the droplet at the droplet centerline is pinned to the defect at the point having maximum negative slope. Simple scaling relations that reflect the influence of defect geometry on the droplet retention force arising from surface tension are able to account for many of the trends observed in the numerical simulations.

1 Introduction

Controlling the motion of liquid droplets on topographically or chemically patterned substrates which are inclined is relevant to a diverse range of applications. Water harvesting from fog utilizes hydrophobic substrates which have hydrophilic topography (such as bumps) to facilitate condensation. The condensed droplets remain pinned at these bumps and coalesce to form larger droplets which eventually depin and slide down into a collection reservoir [1–6]. Droplet-based microfluidic devices have become increasingly popular for high-throughput reaction screenings, point-of-care diagnostics, and single-cell analysis, as they enable precise handling of small volumes of liquids in the form of droplets, making it easy to control chemical and biological reactions. In these devices, topographical patterns are designed on inclined substrates to control droplet pinning, the direction in which the droplet slides after it depins, and other droplet operations such as mixing, splitting, and coalescence. [7–9] Inclined substrates with topographical patterns may also be useful for controlling droplet deposition patterns in inkjet printing by pinning droplets at specific locations. [10,11]

Most substrates have inherent chemical and topographical heterogeneities which lead to the pinning of a droplet on the substrate at non-zero inclination angles. It is often observed that the droplet depins and slides on the substrate with a steady shape and a constant velocity on exceeding a critical inclination angle α_c. This angle can be rationalized by forming a balance between the gravitational force acting on the droplet (which drives depinning), and the retention force due to surface tension acting along the contact line (which resists depinning): [12–17]

$$kBo \sin\alpha_c = \cos\theta_{rcl} - \cos\theta_{acl}, \tag{1.1}$$

where k is a coefficient that generally depends on the droplet shape, surface wettability, and surface topography. It should be noted that sometimes k appears on the right-hand side of (1.1) as a retention-force factor. [15–17] In (1.1), θ_{rcl} is the receding contact angle and θ_{acl} is the advancing contact angle. The Bond number $Bo = \rho g l^2/\sigma$ provides a ratio of gravitational forces to surface-tension forces, where ρ is the liquid density, g is the gravitational acceleration, l is the characteristic length scale of the droplet, and σ is the surface tension.

Motivated by the importance of surface roughness in the applications discussed above, prior experimental works have studied droplet motion on substrates fabricated with topographical microstructures. In general, it is found that the critical inclination angle required to depin a droplet increases with the fraction of the area on the substrate occupied by the microstructures, and the microstructures may also induce stick-slip motion of the droplet.[17–19] Stick-slip motion and other complex behavior have also been observed in prior computational works involving droplets on inclined substrates with multiple topographical defects.[20,21] Prior experimental and theoretical works have shown that chemical patterning can also induce stick-slip motion of droplets on inclined substrates.[22–25]

All the works mentioned above that investigate substrates with topography involve multiple topographical defects. But it is also important to consider the case of a single defect on a substrate to gain fundamental understanding of how the different geometric features of a defect influence droplet motion. While some prior studies have examined how contact-line forces are influenced by single defects[26–28], relatively little work has explored how defect shape affects droplet behavior.[29]

Park and Kumar developed a two-dimensional lubrication-theory-based model to examine a droplet moving on an inclined substrate with a single Gaussian-shaped topographical defect.[29] This modeling approach allows explicit incorporation of surface topography via the defect shape. In addition, a precursor film and disjoining pressure are used to describe the moving contact line, which allows droplet contact angles to be extracted from droplet profiles. This is in contrast to other approaches that have been used in prior works, such as boundary integral methods[30] and diffuse-interface/finite-volume methods[31], where a contact angle hysteresis range needs to be specified to account for surface roughness.

Park and Kumar[29] found that the advancing contact line always pins at the point on the defect that has the maximum negative slope. This maximizes θ_{acl} and, consequently, the retention force in (1.1). Also, the critical inclination angle α_c increases as the defect becomes taller/deeper due to an increase in the retention force, and α_c decreases as the defect becomes wider along the droplet sliding direction due to a decrease in the retention force.

However, most topographical defects, both natural and engineered, are three-dimensional in nature. The width of a three-dimensional defect along the direction lateral to the droplet sliding direction is expected to strongly influence the critical inclination angle at which the droplet pinning-depinning transitions occur, as well as the contact-line pinning location. Thus, whether the observations for two-dimensional situations[29] hold for three-dimensional defects remains a major outstanding question.

To address this issue, we develop a lubrication-theory-based model to study the motion of droplets on inclined substrates with a single three-dimensional topographical defect. Similar to the two-dimensional model discussed above[29], a Gaussian-shaped defect is chosen because it allows us to vary key topographical parameters such as height and width while maintaining a smooth transition from the defect to the flat portions of the substrate. This choice is also motivated by several prior lubrication-theory-based models that have used Gaussian-shaped defects to study the influence of substrate topography on droplet dynamics.[32–35]. It should be noted that fabricating a surface with Gaussian-shaped defects has been demonstrated experimentally.[36] We use a precursor-film/disjoining-pressure approach to model contact-line motion and obtain a nonlinear evolution equation which describes the droplet thickness as a function of position along the substrate and time. The evolution equation is solved numerically. The above methodology yields three-dimensional simulations within the lubrication approximation that allow us to study the influence of defect geometry on droplet dynamics.

The paper is structured as follows. The model formulation is discussed in §2, the influence of defect geometry on droplet dynamics is studied in §3, the locations and shapes of pinned contact lines are examined in §4, and concluding remarks are presented in §5.

2 Mathematical model

A schematic of the problem is shown in figure 1a, where we consider a three-dimensional droplet of a Newtonian liquid moving on an inclined substrate and surrounded by air. Here, r_0 is the initial droplet radius, h_{max} is the initial maximum droplet height, $h(x, y, t)$ is the droplet height, and α is the substrate inclination angle. The coordinates along the substrate are denoted by x and y, and the coordinate normal to the substrate is denoted by z. We consider droplets and defects that are symmetric about the line $y = y_0$, and neglect the dynamics of the surrounding air.

A three-dimensional Gaussian-shaped defect is present at a distance x_d from the leading edge of the droplet. The defect can be in the form of either a bump (Figure 1b), or a dent (Figure 1c), where w_x is the maximum defect width along the x-axis, w_y is the maximum defect width along the y-axis, and h_d is the maximum height or depth of the defect. The defect shape is described by the function $\eta(x, y) = h_d \mathrm{exp}(-[(x - x_c)^2/2w_x^2 + (y - y_c)^2/2w_y^2])$, where (x_c, y_c) is the center with $h_d > 0$ and $h_d < 0$ corresponding to a bump and dent, respectively.

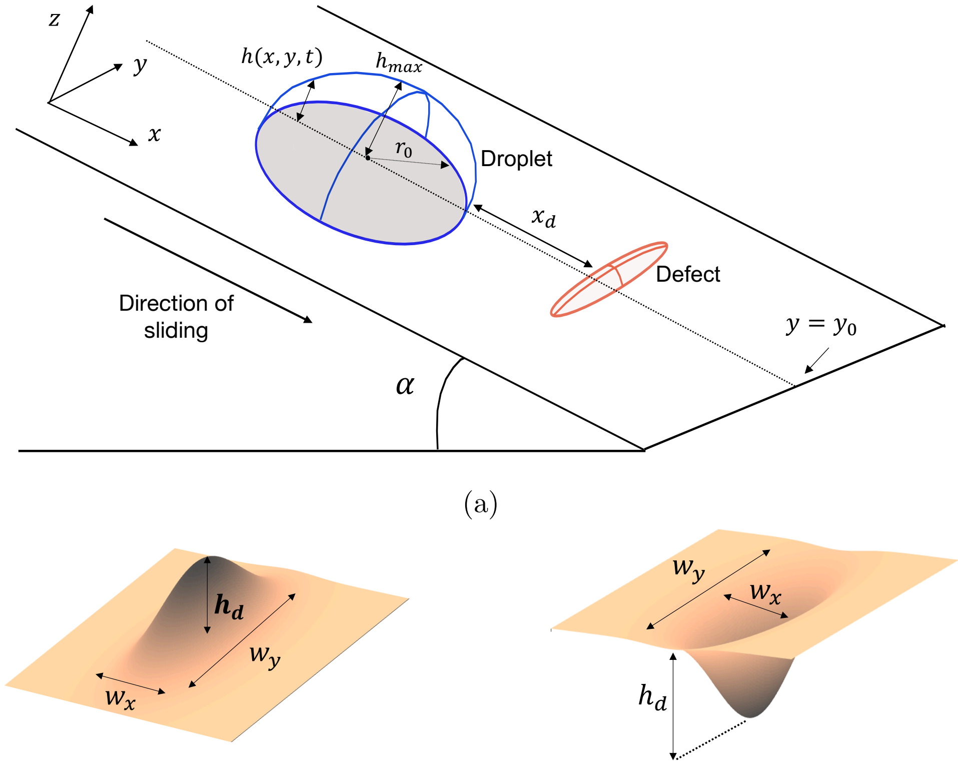

(a)

(b)

(c)

Figure 1: (a) Problem schematic. The defect can be in the form of either a bump (shown) or a dent. The bottom of the droplet is shaded grey. Note that the droplet is not drawn to scale in the schematic. (b) Enlarged view of a bump, where h_d is its maximum height, w_x is its maximum width along the x-axis, and w_y is its maximum width along the y-axis. (c) Enlarged view of a dent, where h_d is its maximum depth.

2.1 Governing equations

We assume that $\epsilon = h_{max}/r_0 \ll 1$, which allows us to invoke the lubrication approximation and simplify the governing equations. We note that lubrication theory has long been used to model droplet behavior, and can provide insight into various experimental observations.[37,38] The characteristic scales for non-dimensionalizing physical quantities are chosen based on prior work.[29,39] The vertical and horizontal distances are non-dimensionalized with h_{max} and r_0, respectively. All stresses are non-dimensionalized with a characteristic capillary pressure $h_{max}\sigma/r_0^2$, where σ is the surface tension. The horizontal velocities in the x- and y-directions are non-dimensionalized with a characteristic capillary speed $u^* = \epsilon^3\sigma/3\mu$, where μ is the droplet viscosity, the vertical velocity is non-dimensionalized with ϵu^*, and time is non-dimensionalized with r_0/u^*. All the variables presented in the paper are dimensionless unless noted otherwise.

At leading order, the mass and momentum balance equations are:

$$u_x + v_y + w_z = 0, \tag{2.1}$$

$$\frac{1}{3}u_{zz} - p_x + G_p = 0, \tag{2.2}$$

$$\frac{1}{3}v_{zz} - p_y = 0, \tag{2.3}$$

$$p_z + G_n = 0, \tag{2.4}$$

where u is the velocity in the x-direction, v is the velocity in the y-direction, w is the velocity in the z-direction, and p is the pressure. Here, $G_p = Bo \sin\alpha/\epsilon$ is the component of the gravitational force parallel to the substrate, $G_n = Bo \cos\alpha$ is the component of the gravitational force normal to the substrate, and $Bo = \rho g r_0^2/\sigma$ is the Bond number, which represents the ratio of gravitational forces to surface-tension forces with ρ representing the droplet density and g denoting the magnitude of the gravitational acceleration. It should be noted that $\epsilon Re \ll 1$ is assumed, where $Re = \rho u^* h_{max}/\mu$ is the Reynolds number.

Motivated by prior work, we model contact-line motion using a precursor-film/disjoining-pressure approach.[32,35,39–41] With this approach, the contact-line position and contact angles are extracted from the droplet height profiles (see §2.2) and are not additional variables. This is in contrast to calculations that impose a slip law on the substrate, which are more complicated to implement because the contact-line position must be determined as part of the solution.[42] A precursor film of thickness b is assumed to be present along the entire substrate, and a two-term disjoining pressure term Π is added to the hydrodynamic pressure p' to describe the total pressure within the droplet as $p = p' + \Pi$, where:

$$\Pi = A\left[\left(\frac{b}{h}\right)^n - \left(\frac{b}{h}\right)^m\right]. \tag{2.5}$$

Here, A is the dimensionless Hamaker constant and h is the droplet thickness. The first term on the right of (2.5) accounts for repulsive intermolecular forces and the second term accounts for attractive intermolecular forces. We choose $n = 3$ and $m = 2$, as previous works show that these values give qualitatively accurate predictions of contact-line motion at a reasonable computational cost.[32,35,39] This approach can readily be extended to model a chemically patterned substrate by spatially varying the Hamaker constant.[40,41]

On a horizontal substrate, the droplet will attain an equilibrium contact angle θ_{eq}, which is related to A:[40]

$$A = \frac{(1-\cos\theta_{eq})(n-1)(m-1)}{b\epsilon^2(n-m)}. \tag{2.6}$$

Here, θ_{eq} is a scaled angle, which is related to the lab-frame angle $\theta_{eq,lab}$ through $\theta_{eq,lab} = \epsilon\theta_{eq}$. All the angles reported in this paper are scaled angles. We specify a θ_{eq} value for our calculations and then use (2.6) to calculate A, which is used in (2.5).

The height of the droplet-air interface relative to $z = 0$ is $H(x, y, t) = h(x, y, t) + \eta(x, y)$, where the following conditions hold:

$$p = -H_{xx} - H_{yy}, \tag{2.7}$$

$$u_z = 0, \tag{2.8}$$

$$v_z = 0, \tag{2.9}$$

$$h_t = w - u\frac{\partial H}{\partial x} - v\frac{\partial H}{\partial y}. \tag{2.10}$$

Here, (2.7) is the normal stress balance, (2.8) is the x-component of the tangential stress balance, (2.9) is the y-component of the tangential stress balance, and (2.10) is the kinematic condition. At the substrate ($z = \eta(x, y)$), we impose the no-slip and no-penetration conditions:

$$u(z=\eta,t) = 0, \qquad v(z=\eta,t) = 0, \tag{2.11}$$

$$w(z=\eta,t) = 0. \tag{2.12}$$

Integrating (2.2), (2.3), and (2.4) with respect to z and using conditions (2.7) - (2.12) yields the droplet height evolution equation:

$$\frac{\partial h}{\partial t} = -\nabla\cdot(h^3\nabla\nabla^2 H) - \nabla\cdot(h^3\nabla\Pi) - G_p\frac{\partial h^3}{\partial x} - \frac{G_n}{2}\nabla\cdot(h^2(H+2\eta)\nabla H). \tag{2.13}$$

We solve (2.13) numerically in the domain $0 \le x \le L_x$ and $0 \le y \le L_y$, and impose the following conditions:

$$h(0,y,t) = b, \qquad h_x(0,y,t) = 0, \tag{2.14}$$

$$h(L_x,y,t) = b, \qquad h_x(L_x,y,t) = 0, \tag{2.15}$$

$$h(x,0,t) = b, \qquad h_y(x,0,t) = 0, \tag{2.16}$$

$$h(x,L_y,t) = b, \qquad h_y(x,L_y,t) = 0, \tag{2.17}$$

which set the precursor film thickness to b on the computational boundary and require it to be flat. For an initial droplet volume v_0, we create an initial condition symmetric about $y = y_0$ in a manner similar to prior work.[39] This is done by first defining $r = \sqrt{(x - x_0)^2 + (y - y_0)^2}$, where (x_0, y_0) is the droplet center. The initial droplet radius is set to r_0, and for all the points in the computational domain that satisfy $r < r_0$, the droplet thickness $h(x, y, 0)$ is given by a fourth-order polynomial $P(r)$ which satisfies the symmetry condition about (x_0, y_0) and the conditions:

$$P(r_0) = b, \qquad P_r(r_0) = 0, \tag{2.18}$$

$$\int_0^{r_0} P(r)\, dr = v_0 + \pi b r_0^2, \tag{2.19}$$

where $\pi b r_0^2$ is the volume of the precursor film in a disk of radius r_0 which is present below the droplet. For all the points in the computational domain that satisfy $r > r_0$, the interface height is defined as $h(x, y, 0) = b$.

An alternating direction implicit (ADI) finite-difference scheme is used to solve (2.13), where second-order centered differences are used for spatial discretization along x and y, and an adaptive time stepping scheme is used for marching the solution forward in time.[43,44] For the simulations presented in this paper, $L_x \times L_y$ ranges from 7×2 to 10×4 to obtain results that are independent of the dimensions of the computational domain. We use 250×250 to 300×300 points per unit area for the spatial discretization. Since our ADI code has a suitable structure for running in parallel, we employ the OpenMP library[45] for parallelization using 24 to 36 CPU cores. As the droplet shape is symmetric about $y = y_0$, the computational domain is halved along the y direction and symmetry conditions are imposed at $y = y_0$ to decrease computational times.

2.2 Contact angles and contact lines

It is convenient to define contact angles and contact-line positions by considering the cross section of the droplet profile in the plane at $y = y_0$ (Figure 1a). For a perfectly flat substrate, we define apparent advancing (θ_{acl}) and receding (θ_{rcl}) contact angles (Figure 2a) as the largest angles between the substrate and the tangents to the droplet-air interface, on the advancing and receding sides of the droplet. We define the advancing and receding contact-line locations, x_{acl} and x_{rcl}, as the points where the tangents corresponding to θ_{acl} and θ_{rcl}, and the substrate,

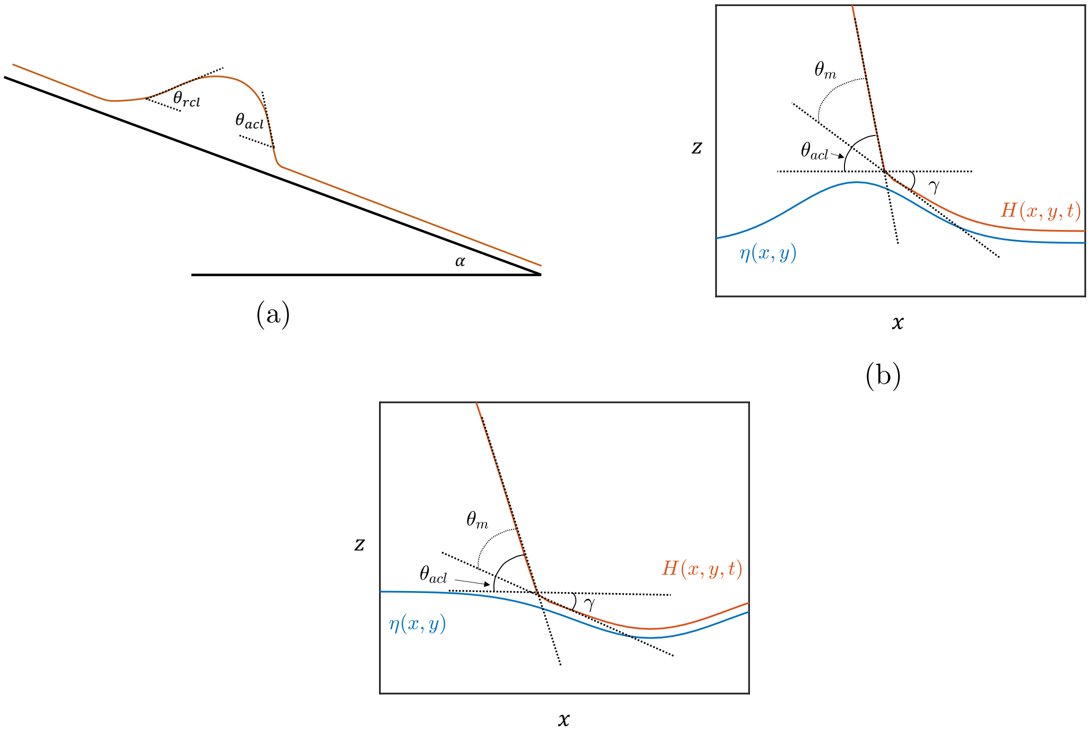

(a)

(b)

(c)

Figure 2: (a) Sideview of the x-z plane at $y = y_0$ for a substrate without any defects. Note that the droplet is not drawn to scale in the schematic. (b) Enlarged side view of the x-z plane at $y = y_0$ showing the contact-line region when the advancing contact line moves over a bump, where η is the defect height, H is the interface height, θ_{acl} is the apparent advancing contact angle, θ_m is the mesoscopic angle, and γ is the slope of the bump at the point where it coincides with the contact line. (c) Enlarged sideview of the contact-line region when the advancing contact line moves over a dent.

intersect. For a substrate with zero inclination and a symmetric droplet shape, $\theta_{acl} = \theta_{rcl} = \theta$. If $\theta > \theta_{eq}$, the droplet will spread until $\theta = \theta_{eq}$, and if $\theta < \theta_{eq}$, the droplet will retract until $\theta = \theta_{eq}$. Although contact angles and contact-line positions can certainly be defined at other values of y, using the values at $y = y_0$ is convenient for characterizing droplet behavior given the symmetry of the problem.

To ensure that the droplet attains the specified θ_{eq}, separate simulations are performed on a horizontal substrate where the initial condition is marched ahead in time until the droplet reaches a steady shape. The value of A is tuned such that the θ_{acl} calculated from the resulting steady shape is approximately equal to θ_{eq} (within 1^o).

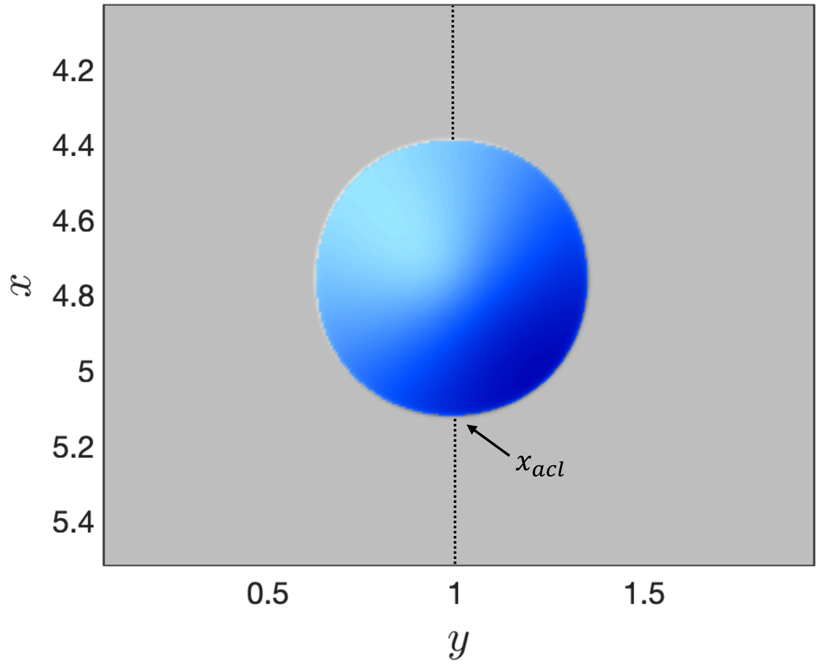

Figure 3: Top view of the x-y plane showing a circular droplet shape and x_{acl} for $t = 15$ on a perfectly flat substrate. The parameters are $v_0 = 1.66$, $b = 0.005$, $A = 6932.4$ ($\theta_{eq} = 45^o, \epsilon = 0.13$), $Bo = 2$, $h_d = 0$, and $\alpha = 30^o$. The initial condition is centered at $(1.2, 1)$ with $r_0 = 0.75$.

For a substrate with a topographical defect, we define a mesoscopic contact angle θ_m[32] (Figures 2b and 2c):

$$\tan\theta_m = \frac{h_x}{1 + (h_x + \eta_x)h_x}. \tag{2.20}$$

The angles θ_{acl} and θ_{rcl} are calculated by identifying the points on the advancing and receding sides of the interface where θ_m has the largest magnitude, and extrapolating the tangents at these points to the substrate. The advancing and receding contact-line positions x_{acl} and x_{rcl} are defined as the points where these tangents intersect the substrate.

2.3 Model validation

The model is validated by performing simulations with a perfectly flat inclined substrate and comparing our results with prior work. Podgorski *et al.*[46] performed experiments to study droplet motion on an inclined substrate. They found that below a critical value of the substrate inclination angle α (which depends on the droplet volume), the droplet attains a steady shape with a circular footprint and slides with a terminal speed that increases with the substrate inclination angle. Lubrication-theory-based models[47,48], including one developed by Espín and Kumar[39], are able to qualitatively reproduce this behavior.

We perform simulations for a three-dimensional droplet sliding down a perfectly flat inclined substrate using the parameter values in the calculations of Espín and Kumar[39] (listed in the caption of figure 3) for a case where the droplet has a circular footprint. Figure 3 shows the top view of the steady shape attained by the droplet and the arrow indicates the position of the advancing contact line x_{acl}. The dimensionless terminal droplet speed v_t is calculated by obtaining the slope of x_{acl} vs. t. Using a dimensional terminal speed of $v = u^* v_t$, the corresponding capillary number is calculated as $Ca = \mu v/\sigma = \epsilon^3 v_t/3$. The calculations show that Ca increases linearly with $Bo \sin\alpha$ ($Bo = 2$ is fixed and α is varied), indicating that the terminal speed increases with substrate inclination. This is qualitatively consistent with the experiments by Podgorski *et al.*[46]., where a linear increase is also observed. As noted in Espin and Kumar[39], obtaining quantitative agreement would likely require using a much smaller precursor-film thickness, which is computationally prohibitive.

A precursor film thickness of $b = 0.005$ is used in the above calculations, as it provides a qualitatively accurate description of contact-line motion at a reasonable computational cost. Smaller θ_{eq} values lead to slower terminal sliding speeds due to more viscous dissipation[49,50], but do not change the qualitative nature of the results. For the rest of the paper, we fix the values of b, A (θ_{eq}), v_0, and r_0 to those specified in figure 3 as we want to isolate the influence of defect geometry on droplet dynamics. For calculations where a defect is present, the defect is placed at a distance $x_d = 1.2$-1.5 from the leading edge of the initial droplet shape, which provides a sufficient distance for the droplet to attain a steady circular shape before it encounters the defect.

Experiments by Podgorski *et al.*[46] also showed that the droplet undergoes wetting transitions as α increases. The droplet has a nearly circular footprint for lower α values, attains a teardrop-like shape as α increases, and undergoes "pearling" at even larger α values, where the receding end of the droplet stretches into a liquid neck and smaller droplets break-off from the neck due to a Rayleigh-Plateau-like instability. These wetting transitions have been qualitatively reproduced by prior lubrication-theory-based models.[39,47,48] Our calculations are able to reproduce these transitions as well. For all further calculations, we use $Bo < 4$ (with the other parameter values specified in figure 3), as this leads to a nearly circular droplet shape for most α values, which allows us to isolate the influence of the defect geometry on droplet dynamics.

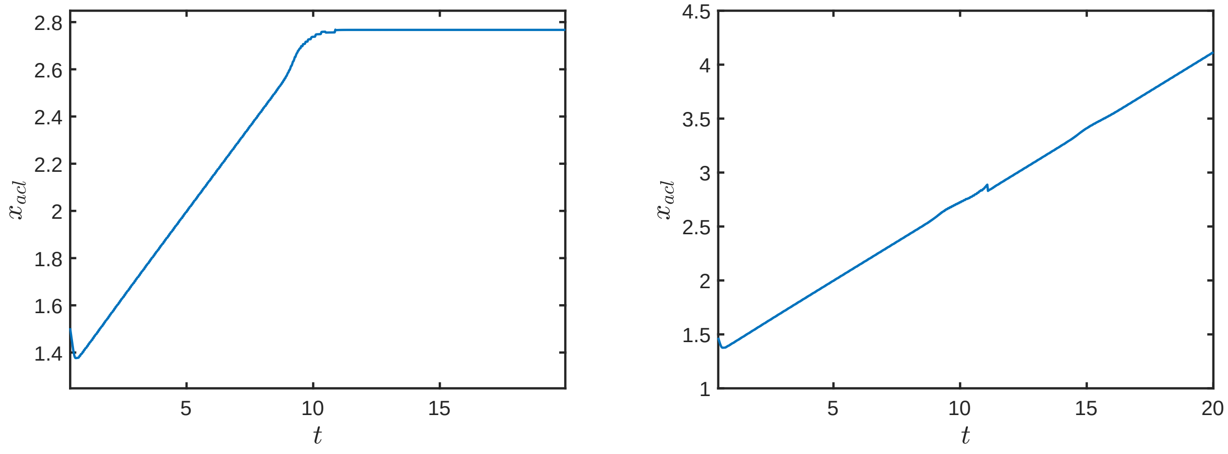

(a)

(b)

Figure 4: (a) x_{acl} vs. t for $\alpha = 30^o$. (b) x_{acl} vs. t for $\alpha = 50^o$. The kinks at $t \approx 11$ arise while numerically resolving x_{acl} from droplet profiles. The parameters are $v_0 = 1.66$, $b = 0.005$, $A = 6932.4$ ($\theta_{eq} = 45^o, \epsilon = 0.13$), $Bo = 2$, $w_y = 0.075$, $h_d = 0.025$, and $w_x = 0.05625$. The initial condition is centered at $(1.2, 1)$ with $r_0 = 0.75$.

3 Influence of defect geometry on droplet dynamics

3.1 Influence of maximum lateral width

Figure 4a shows x_{acl} vs. t for a bump-type defect with a maximum lateral width of $w_y = 0.075$ and $\alpha = 30^o$. Initially, x_{acl} decreases with t as the droplet attains the specified θ_{eq}. Following this, x_{acl} increases with t until it reaches $x_{acl} = 2.79$, after which it remains constant, indicating that the droplet slides until it reaches the defect and remains pinned there. Figure 4b shows x_{acl} vs. t for $w_y = 0.075$ and $\alpha = 50^o$. Here, x_{acl} increases with t following the initial decrease, indicating that the droplet does not pin at the defect and slides freely. Similar behavior is also seen for a dent-type defect. These observations indicate that there is a critical inclination angle α_c above which droplet depinning occurs.

To determine α_c for a given defect shape, α is increased in fixed intervals until the droplet depins and slides freely (x_{acl} vs. t similar to figure 4b). Since these calculations are computationally expensive, it is not feasible to vary α in very small intervals, so α is increased in intervals of 5°-12°. As discussed in §2.3, the value of θ_{eq} is fixed for all the calculations to isolate the influence of defect geometry. Increasing θ_{eq} increases the retention force[29], which

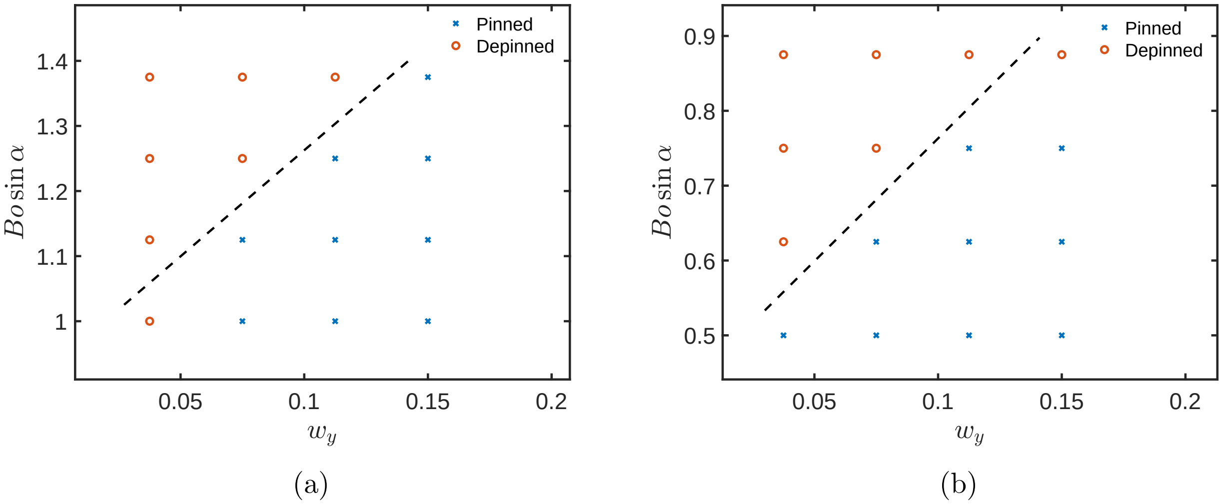

Figure 5: Parameter maps of $Bo\sin\alpha$ vs. w_y for a (a) bump ($h_d = 0.02$) and (b) dent ($h_d = -0.02$). Red circles indicate depinned droplets and blue crosses indicate pinned droplets. The dashed straight lines are placed such that they almost entirely separate the pinned and depinned states, consistent with $Bo\sin\alpha \sim w_y$ from (3.2). The parameters are $v_0 = 1.66$, $b = 0.005$, $A = 6932.4$ ($\theta_{eq} = 45^o, \epsilon = 0.13$), $Bo = 2$, and $w_x = 0.05625$. The initial condition is centered at $(1.2, 1)$ with $r_0 = 0.75$.

increases α_c, but changing θ_{eq} does not change the qualitative nature of the influence of defect geometry on α_c.

Figures 5a and 5b show parameter maps of $Bo\sin\alpha$ vs. w_y for a bump and a dent, where α is increased in intervals of 5° while fixing $Bo = 2$ for each w_y value. The blue crosses show the cases where the droplet remains pinned at the defect and the red circles show the cases where the droplet depins and slides freely. It can be seen that as w_y increases, the transition from droplet pinning to depinning occurs at a larger α_c value.

A scaling relation for α_c can be derived to rationalize the results from numerical simulations. Gravitational forces acting on the droplet drive depinning, whereas the forces arising near the advancing contact line due to disjoining-pressure gradients resist depinning.[32,35] This resisting force is estimated by multiplying the disjoining pressure near the contact line, Π_{cl}, with an approximate projected area of the defect perpendicular to the x-axis. The dimensional force balance is given by:

$$\rho v_0 g \sin\alpha_c \sim w_y' h_d' \Pi_{cl}', \tag{3.1}$$

where primes represent dimensional values.

Non-dimensionalizing w'_y with r_0, h'_d with h_{max}, and Π'_{cl} with $h_{max}\sigma/r_0^2$ yields the dimensionless force balance:

$$\frac{Bo\sin\alpha_c}{\epsilon} \sim w_y h_d \Pi_{cl}. \tag{3.2}$$

For (1.1), values of the receding (θ_{rcl}) and the advancing (θ_{acl}) contact angles are required to estimate the retention force, and consequently α_c. In contrast, (3.2) does not require the contact angle values and explicitly incorporates the influence of the lateral width w_y and height h_d of the defect on α_c. According to (3.2), $Bo\sin\alpha_c$ varies linearly with w_y, which is consistent with the numerical simulations, as straight lines can be used to almost entirely separate the cases of pinned and depinned droplets for both bumps and dents in the parameter maps of figure 5.

The three-dimensional model presented here explicitly accounts for the influence of the lateral defect width w_y on the critical inclination angle α_c through (3.2), which is a significant advance over prior work, which focused on two-dimensional situations.[29]. Here, increasing w_y increases the retention force, which increases α_c.

3.2 Influence of maximum defect height

Figure 6 shows a parameter map of $Bo\sin\alpha$ vs. the maximum defect height h_d, where α is increased in intervals of 12° while fixing $Bo = 2$ for each h_d value. For a flat substrate ($h_d = 0$), the droplet slides for any non-zero inclination angle ($\alpha \approx 1^\circ$, yellow triangle in figure 6), which is expected as surface roughness is not accounted for in any way. For a non-flat substrate, the blue crosses show the cases where the droplet remains pinned at the defect and the red circles show the cases where the droplet depins and slides freely. It can be seen that the transition from droplet pinning to depinning occurs at a larger α_c, as a bump becomes taller (h_d increases for $h_d > 0$), and as a dent becomes deeper (h_d decreases for $h_d < 0$).

The findings discussed above can also be rationalized using (3.2). Here, $Bo\sin\alpha$ varies linearly with h_d. This is consistent with the numerical simulations, as straight lines can be used to completely separate the cases of pinned and depinned droplets for the bump (dotted line) and the dent (dashed line) in figure 6. Thus, as the defect becomes taller/deeper, the retention force acting on the droplet increases, which causes depinning at a higher α_c.

For two-dimensional geometries,[29] making the defect taller/deeper increases α_c. We have shown here that this conclusion also holds in three dimensions. However, for two-dimensional defects this conclusion was rationalized by showing that increasing h_d increases θ_{acl}, which increases the retention force in (1.1), causing depinning at a larger α_c.[29] In contrast, the scaling relationship (3.2) developed here explicitly accounts for the defect geometry and does not require contact-angle values.

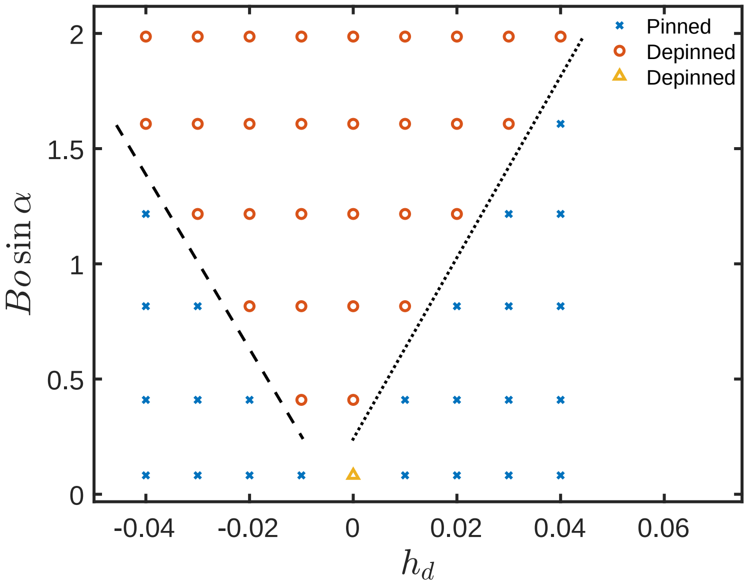

Figure 6: Parameter map of $Bo\sin\alpha$ vs. h_d. The dashed and dotted straight lines are used to separate pinned and depinned droplets for a dent and bump, respectively, following (3.2). The parameters are $v_0 = 1.66$, $b = 0.005$, $A = 6932.4$ ($\theta_{eq} = 45^o, \epsilon = 0.13$), $Bo = 2$, $w_y = 0.075$, and $w_x = 0.05625$. The initial condition is centered at $(1.2, 1)$ with $r_0 = 0.75$.

3.3 Influence of maximum width along droplet sliding direction

Figures 7a and 7b show parameter maps of $Bo\sin\alpha$ vs. the maximum defect width along the droplet sliding direction, w_x, for a bump and a dent. Here, α is increased in intervals of 5° while fixing $Bo = 2$ for each w_x value. The blue crosses show the cases where the droplet remains pinned at the defect and the red circles show the cases where the droplet depins and slides freely. The dashed lines serve as visual guides to separate pinned and depinned droplets. It can be seen that for both a bump and a dent, the transition from droplet pinning to depinning occurs at a lower α_c for a larger w_x. In (3.2), the disjoining pressure near the advancing contact line is multiplied with the approximate projected area of the defect perpendicular to the x-axis to obtain the retention force. This projected area does not depend on w_x, making it difficult to obtain a simple scaling law relating α_c to w_x.

Nevertheless, the trends observed in figures 7a and 7b can be understood by using (1.1) to calculate the influence of w_x on the retention force, where the values of θ_{rcl} and θ_{acl} are now required. It can be seen from figures 2b and 2c that at the axis of symmetry $y = y_0$, the

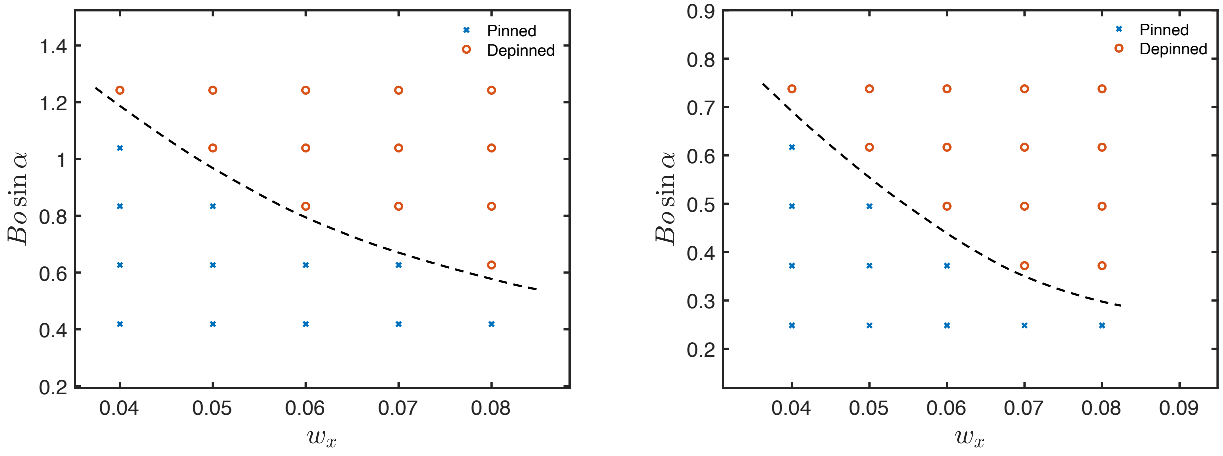

(a) (b)

Figure 7: Parameter maps of $Bo \sin \alpha$ vs. w_x for a (a) bump ($h_d = 0.02$) and (b) dent ($h_d = -0.02$). The dashed lines serve as visual guides to separate pinned and depinned droplets. The parameters are $v_0 = 1.66$, $b = 0.005$, $A = 6932.4$ ($\theta_{eq} = 45^o, \epsilon = 0.13$), $Bo = 2$, and $w_y = 0.075$. The initial condition is centered at $(1.2, 1)$ with $r_0 = 0.75$.

following geometric relation holds at the pinned advancing contact line for both a bump and a dent:

$$\theta_{acl} = \theta_m + \gamma, \tag{3.3}$$

where γ is the slope along the defect at the point where the advancing contact line pins.

Our calculations show that for all the cases of a pinned droplet, $\theta_m \approx \theta_{eq}$ and θ_{rcl} does not vary significantly ($\approx 4\%$) with w_x. Additionally, the advancing contact line always pins at the point on the defect that has the maximum negative slope γ_{max} in the plane at $y = y_0$. As a consequence of this pinning location, $\theta_{acl} \approx \theta_{eq} + \gamma_{max}$ is maximized, which maximizes the retention force in (1.1). A more detailed discussion about the location of the pinned contact line is presented in §4. It can be seen from figures 1b and 1c that γ_{max} decreases as w_x increases. As a result, θ_{acl} decreases as w_x increases, which decreases the retention force in (1.1), and consequently the droplet depins at a lower α_c.

For two-dimensional defects[29], it has been found that making the defect wider along the droplet sliding direction decreases θ_{acl}, which decreases the retention force (from (1.1)) and causes depinning at a lower α_c. The results presented here demonstrate that this conclusion also holds in three dimensions.

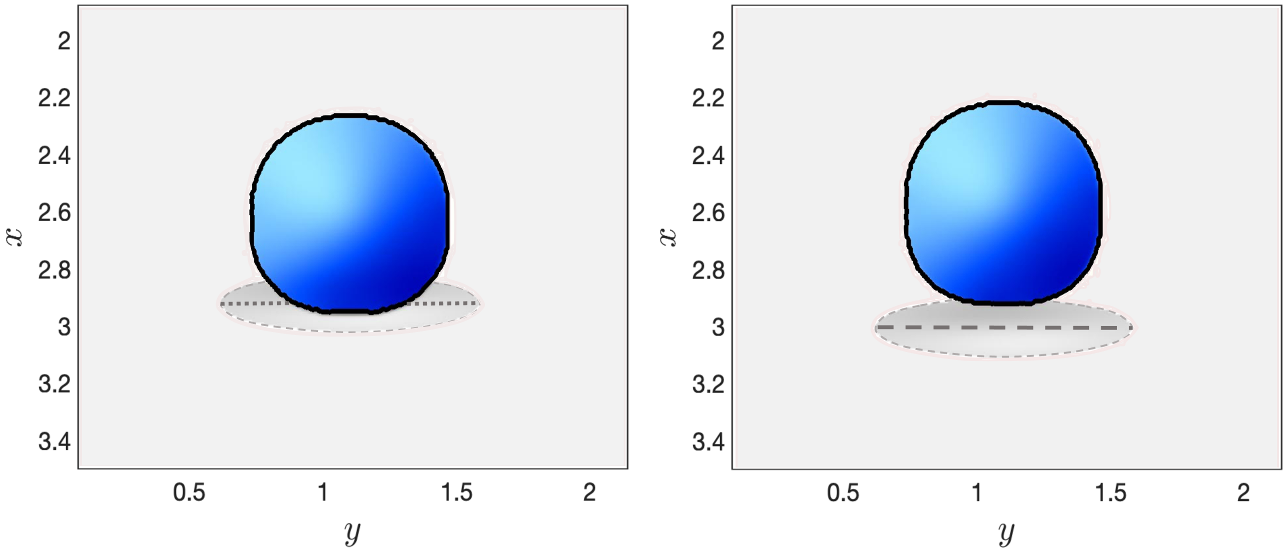

(a) (b)

Figure 8: Top views of pinned droplets for a (a) bump ($h_d = 0.02$) and (b) dent ($h_d = -0.02$). The region where the droplet thickness is greater than the precursor-film thickness ($h > b$) is marked in blue. The contact lines are marked by the solid black curves. The parameters are $v_0 = 1.66$, $b = 0.005$, $A = 6932.4$ ($\theta_{eq} = 45^o, \epsilon = 0.13$), $Bo = 2$, $w_y = 0.15$, $w_x = 0.05625$, and $\alpha = 10^o$. The initial condition is centered at $(1.2, 1)$ with $r_0 = 0.75$.

We have tried to calculate the value of the retention-force factor (k appearing on the right-hand side in (1.1)) by extracting the values of $Bo \sin \alpha_c$, θ_{rcl}, and θ_{acl} from all the calculations presented in §3, and fitting a straight line to $Bo \sin \alpha_c$ vs. $\cos \theta_{rcl} - \cos \theta_{acl}$ (see supplementary information). The numerical simulations do not agree well with the linear fit. This likely happens because k is assumed to be a constant in (1.1), but the value of k is expected to depend on the defect dimensions, which are different for all the numerical simulations.

4 Location and shape of pinned contact line

Besides the critical inclination angle, another feature of fundamental interest is the location and shape of the pinned contact line. Figures 8a and 8b show top views of pinned droplets for a bump and a dent, where the contact lines are marked by the solid black curves. For a bump, it is seen that the contact line at the droplet front is located on the downhill side of the bump. For a dent, it is seen that the contact line at the droplet front is located on the downhill side

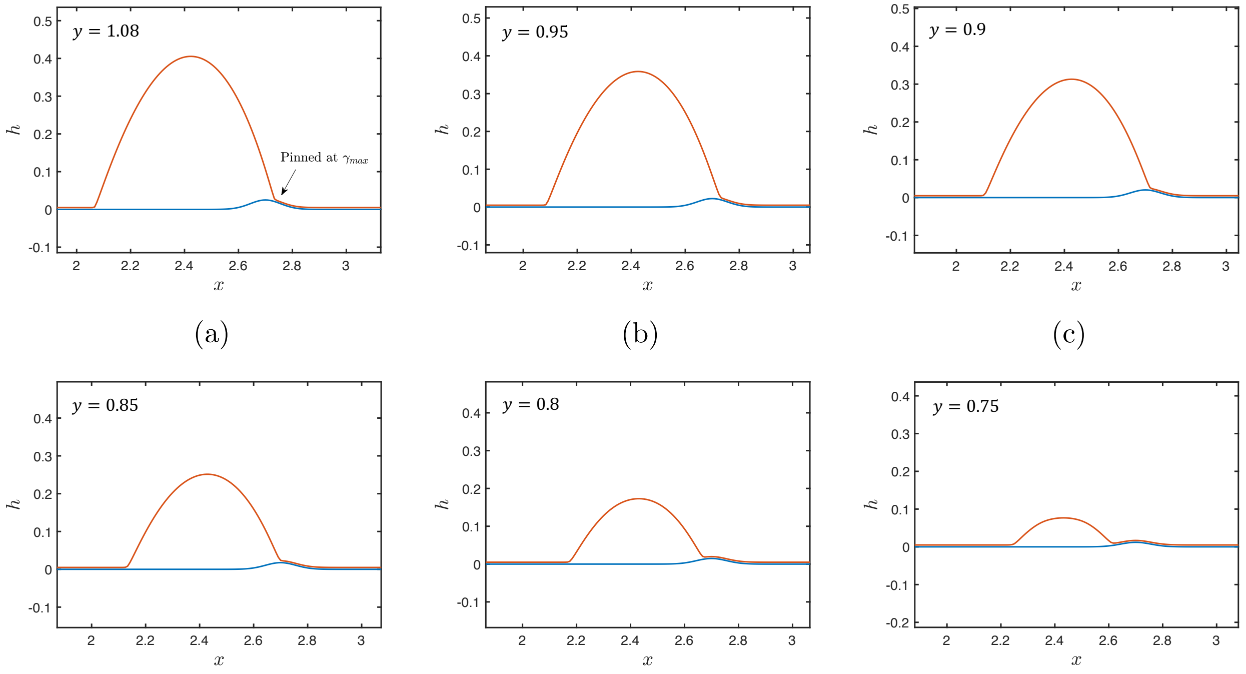

(a) (b) (c)

(d) (e) (f)

Figure 9: Cross-section view in the x-z plane of a droplet pinned at a bump for (a) $y = 1.08$ (axis of symmetry) (b) $y = 0.95$ (c) $y = 0.9$ (d) $y = 0.85$ (e) $y = 0.8$ and (f) $y = 0.75$. The red lines show the droplet profile and the blue lines show the defect shape. The parameters are $v_0 = 1.66$, $b = 0.005$, $A = 6932.4$ ($\theta_{eq} = 45^o, \epsilon = 0.13$), $Bo = 2$, $w_y = 0.075$, $h_d = 0.02$, $w_x = 0.05625$, and $\alpha = 10^o$. The initial condition is centered at $(1.2, 1)$ with $r_0 = 0.75$.

of the dent. These features can be understood by examining how the pinning location varies in the y-direction.

Figure 9 shows the cross sections of droplet profiles in the x-z plane for different y values for the pinned droplet in figure 8a. At the axis of symmetry ($y = y_0$), the advancing contact line pins at the point of maximum negative slope γ_{max} on the defect (Figure 9a). As discussed in §3.3, θ_{acl} and consequently the retention force in (1.1), are maximized at this pinning location. But the contact-line location does not coincide with the maximum negative slope for $y \neq y_0$, and is shifted to the left as y moves further from y_0 (Figures 9b-9f).

Figure 10 shows the droplet cross sections for different y values for the pinned droplet in figure 8b. Similar to the bump, the advancing contact line at $y = y_0$ pins at the point on the dent that has the maximum negative slope γ_{max} (Figure 10a). Since γ_{max} lies on the downhill

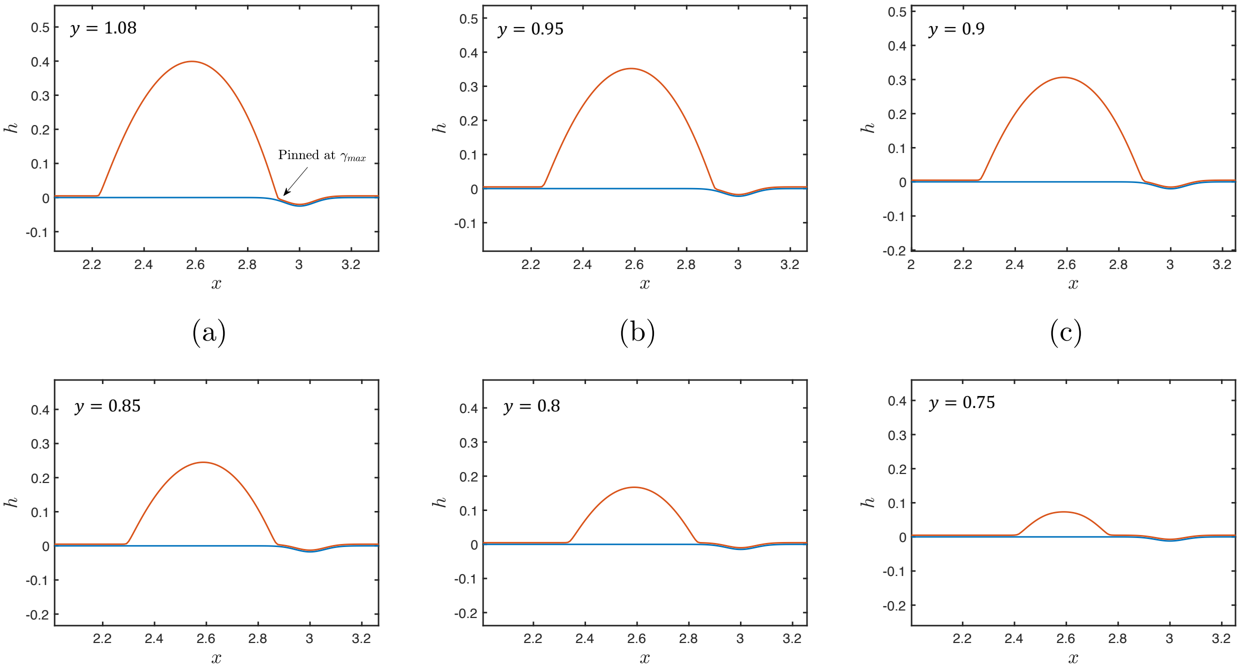

(a) (b) (c)

(d) (e) (f)

Figure 10: Cross-section view in the x-z plane of a droplet pinned at a dent for (a) $y = 1.08$ (axis of symmetry) (b) $y = 0.95$ (c) $y = 0.9$ (d) $y = 0.85$ (e) $y = 0.8$ and (f) $y = 0.75$. The red lines show the droplet profile and the blue lines show the defect shape. The parameters are $v_0 = 1.66$, $b = 0.005$, $A = 6932.4$ ($\theta_{eq} = 45^o, \epsilon = 0.13$), $Bo = 2$, $w_y = 0.075$, $h_d = -0.02$, $w_x = 0.05625$, and $\alpha = 10^o$. The initial condition is centered at $(1.2, 1)$ with $r_0 = 0.75$.

side of the dent, the contact line covers a smaller portion of the dent compared to the bump, where the maximum negative slope lies on the downhill side of the bump. As with the bump, the pinning location does not coincide with the maximum negative slope for $y \neq y_0$, and is shifted to the left as y moves further from y_0 (Figures 10b-10a).

We now characterize contact-line shapes for the pinned droplets discussed above. Figures 11a and 11b show these shapes in the advancing half of the droplet for a bump and a dent, and the dashed red lines show the location of the maximum negative slope along the defects. For both cases, it can be seen that the contact line coincides with the maximum negative slope only at the axis of symmetry. Figures 11c and 11d show the shapes of the pinned contact lines (solid blue lines) and the steady circular profiles attained by the droplet before encountering the defects (dashed red lines) for a bump and dent. For both cases, it can be seen that the

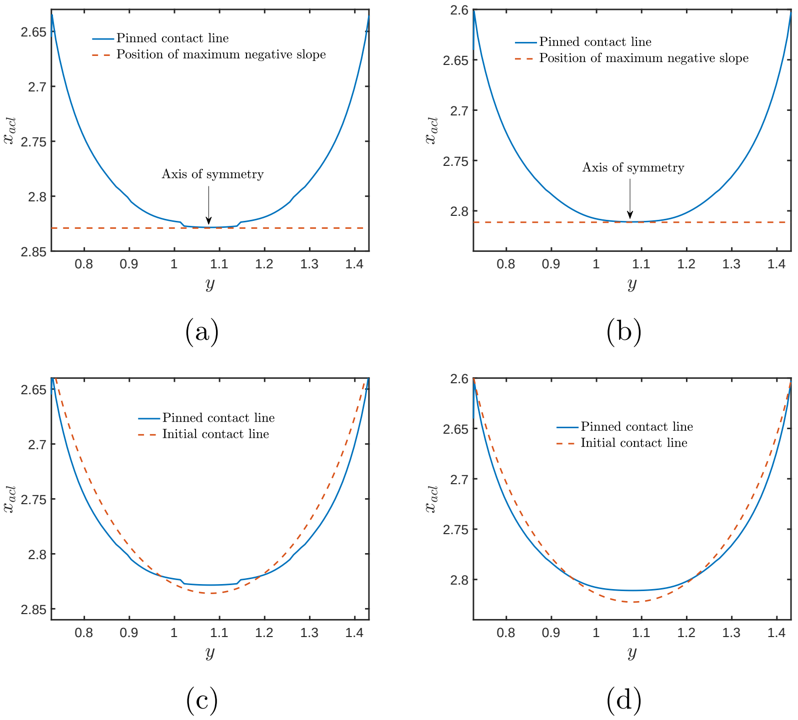

(a) (b) (c) (d)

Figure 11: (a) x_{acl} vs. y for a droplet pinned at a bump ($h_d = 0.02$). The two kinks at $y = 1.04$ and $y = 1.14$ arise while numerically resolving x_{acl} from the droplet profiles at the top of the bump. (b) x_{acl} vs. y for a droplet pinned at a dent ($h_d = -0.02$). The dashed red lines in above figures show the position of the maximum negative slope γ_{max} along the defect. (c) x_{acl} vs. y for a droplet pinned at a bump ($h_d = 0.02$). (d) x_{acl} vs. y for a droplet pinned at a dent ($h_d = -0.02$). The dashed red lines show the shape of the droplet contact line before it encounters the defect (the initial contact-line position has been translated so that it overlaps the pinned contact-line position). The other parameters are the same as in figure 8.

shape of the pinned contact line is more blunt than the circular profile as a consequence of liquid "piling up" at the droplet front.

Our results show that for the three-dimensional defects considered here, pinning occurs at the point of maximum negative slope only at the axis of symmetry. This behavior is more complicated than what might be inferred from results for two-dimensional systems, which indicate that pinning simply occurs at the point of maximum negative slope.[29] In addition, our three-dimensional calculations illustrate how contact-line shape is influenced by a defect. Although we have considered symmetric bumps and dents, we anticipate that for other geometries pinning will also occur at the point of maximum negative slope at the leading edge of the droplet and the contact-line shape will be more blunt.

5 Conclusions

We have developed a lubrication-theory-based model to study the pinning-depinning transition of circular droplets on an inclined substrate with a three-dimensional topographical defect. A single topographical defect is considered to isolate the influence of defect geometry on droplet dynamics. Park and Kumar[29] developed a lubrication-theory-based model to examine a droplet sliding on an inclined substrate with a single two-dimensional defect. Whether their observations hold in three dimensions remains a major open question, and this issue is addressed in our work.

The droplet remains pinned at the defect below a critical substrate inclination angle α_c. Above α_c, the gravitational forces acting on the droplet exceed the retention forces due to surface tension, and the droplet depins and slides freely. For a two-dimensional defect, increasing the height/depth of the defect increases α_c due to an increase in the retention force, and increasing the width of the defect decreases α_c due to a decrease in the retention force.[29] Here, we have shown that these conclusions hold in three dimensions. We have also shown that increasing the lateral width of the defect increases α_c due to an increase in the retention force. This work significantly advances physical understanding by explicitly accounting for the influence of defect geometry on the retention force, and consequently α_c, through (3.2).

For the case of a droplet pinned at a two-dimensional defect, it was observed that the advancing contact line pins at the point of maximum negative slope, as this maximizes the retention force.[29] We have shown that this observation only holds at the axis of symmetry in three dimensions. Our three-dimensional calculations also demonstrate that the contact line has an approximately circular shape which is more blunt due to liquid piling up near the defect. A key advantage of the lubrication-theory-based model used here is that it can readily be extended to investigate more complex scenarios where the substrate may have multiple defects of different shapes or chemical heterogeneity. Droplet pinning can be influenced by substrate stiffness as well[51], and situations involving deformable substrates can also be studied using lubrication-theory-based models.[52,53] In addition, our lubrication-theory-based model serves as motivation for numerical simulations that relax the lubrication approximation, and can be used to help validate such simulations.

Conflicts of interest

There are no conflicts of interest to declare.

Acknowledgments

This material is based upon work supported by the National Science Foundation under Grant No. CBET-1935968. We thank L Espín for helpful discussions.

References

1 W. Shi, M. Anderson, J. Tulkoff, B. Kennedy and J. Boreyko, *ACS Applied Materials & Interfaces*, 2018, **10**, 11979–11986.

2 S. Korkmaz and I. Kariper, *Environmental Chemistry Letters*, 2020, **18**, 361–375.

3 Z. Yu, T. Zhu, J. Zhang, M. Ge, S. Fu and Y. Lai, *Advanced Functional Materials*, 2022, **32**, 2200359.

4 S. Brindhu and P. Viswanath, *Langmuir*, 2021, **37**, 8281–8289.

5 X. Chen, X. Wu, F. Li, X. Zhao and S. Wang, *Nano*, 2021, **16**, 2150086.

6 L. Zhai, M. Berg, F. Cebeci, Y. Kim, J. Milwid, M. Rubner and R. Cohen, *Nano Letters*, 2006, **6**, 1213–1217.

7 Y. Zeng, J. Khor, T. van Neel, W. Tu, J. Berthier, S. Thongpang, E. Berthier and A. Theberge, *Nature Reviews Chemistry*, 2023, **7**, 439–455.

8 K. Churski, P. Korczyk and P. Garstecki, *Lab on a Chip*, 2010, **10**, 816–818.

9 R. Seemann, M. Brinkmann, T. Pfohl and S. Herminghaus, *Reports on Progress in Physics*, 2011, **75**, 016601.

10 I. Arango, L. Bonil, D. Posada and J. Arcila, *International Journal on Interactive Design and Manufacturing (IJIDeM)*, 2019, **13**, 967–980.

11 B. Ping, J. Huang and F. Meng, *The International Journal of Advanced Manufacturing Technology*, 2023, **127**, 3371–3384.

12 G. Macdougall and C. Ockrent, *Proceedings of the Royal Society of London. Series A. Mathematical and Physical Sciences*, 1942, **180**, 151–173.

13 C. Furmidge, *Journal of Colloid Science*, 1962, **17**, 309–324.

14 E. Dussan and R. Chow, *Journal of Fluid Mechanics*, 1985, **151**, 20.

15 A. ElSherbini and A. Jacobi, *Journal of Colloid and Interface Science*, 2006, **299**, 841–849.

16 N. Gao, F. Geyer, D. Pilat, S. Wooh, D. Vollmer, H. Butt and R. Berger, *Nature Physics*, 2018, **14**, 191–196.

17 S. Humayun, R. Maynes, J. Crockett and B. Iverson, *Langmuir*, 2022, **38**, 15960–15972.

18 C. Lv, C. Yang, P. Hao, F. He and Q. Zheng, *Langmuir*, 2010, **26**, 8704–8708.

19 M. Kumar, R. Bhardwaj and K. Sahu, *Langmuir*, 2019, **35**, 2957–2965.

20 N. Savva and S. Kalliadasis, *Journal of Fluid Mechanics*, 2013, **725**, 462–491.

21 Y. Tsao, Y. Liao and H. Tsao, *Physics of Fluids*, 2023, **35**, 122121.

22 J. Joanny and M. Robbins, *The Journal of Chemical Physics*, 1990, **92**, 3206–3212.

23 S. Varagnolo, D. Ferraro, P. Fantinel, M. Pierno, G. Mistura, G. Amati, L. Biferale and M. Sbragaglia, *Physical Review Letters*, 2013, **111**, 066101.

24 S. Varagnolo, V. Schiocchet, D. Ferraro, M. Pierno, G. Mistura, M. Sbragaglia, A. Gupta and G. Amati, *Langmuir*, 2014, **30**, 2401–2409.

25 Q. Li, Y. Liu, B. He and B. Wen, *Langmuir*, 2023, **39**, 14487–14499.

26 J. Joanny and P. De Gennes, *The Journal of Chemical Physics*, 1984, **81**, 552–562.

27 E. Raphael and P. De Gennes, *The Journal of Chemical Physics*, 1989, **90**, 7577–7584.

28 A. Saal, B. Straub, H. Butt and R. Berger, *Europhysics Letters*, 2022, **139**, 47001.

29 J. Park and S. Kumar, *Langmuir*, 2017, **33**, 7352–7363.

30 P. Dimitrakopoulos and J. Higdon, *Journal of Fluid Mechanics*, 1999, **395**, 181–209.

31 H. Ding, P. Spelt and C. Shu, *Journal of Computational Physics*, 2007, **226**, 2078–2095.

32 L. Espín and S. Kumar, *Journal of Fluid Mechanics*, 2015, **784**, 465–486.

33 T. Pham and S. Kumar, *Langmuir*, 2017, **33**, 10061–10076.

34 T. Pham and S. Kumar, *Physical Review Fluids*, 2019, **4**, 034004.

35 V. Charitatos, T. Pham and S. Kumar, *Physical Review Fluids*, 2021, **6**, 084001.

36 R. Lhermerout and K. Davitt, *Soft Matter*, 2018, **14**, 8643–8650.

37 A. Oron, S. Davis and S. Bankoff, *Reviews of Modern Physics*, 1997, **69**, 931.

38 S. Kumar and V. Charitatos, *Langmuir*, 2022, **38**, 15889–15904.

39 L. Espín and S. Kumar, *Physical Review Fluids*, 2017, **2**, 014004.

40 L. Schwartz and R. Eley, *Journal of Colloid and Interface Science*, 1998, **202**, 173–188.

41 L. Schwartz, *Langmuir*, 1998, **14**, 3440–3453.

42 N. Savva and S. Kalliadasis, *Europhysics Letters*, 2011, **94**, 64004.

43 T. Witelski and M. Bowen, *Applied Numerical Mathematics*, 2003, **45**, 331–351.

44 M. Mata and A. Bertozzi, *Journal of Computational Physics*, 2011, **230**, 6334–6353.

45 OpenMP Architecture Review Board, *OpenMP Application Programming Interface*, OpenMP ARB, 5th edn, 2022.

46 T. Podgorski, J. Flesselles and L. Limat, *Physical Review Letters*, 2001, **87**, 036102.

47 L. Schwartz, D. Roux and J. Cooper-White, *Physica D: Nonlinear Phenomena*, 2005, **209**, 236–244.

48 G. Ahmed, M. Sellier, M. Jermy and M. Taylor, *European Journal of Mechanics-B/Fluids*, 2014, **48**, 218–230.

49 H. Kim, H. Lee and B. Kang, *Journal of Colloid and Interface Science*, 2002, **247**, 372–380.

50 E. Benilov and M. Benilov, *Journal of Fluid Mechanics*, 2015, **773**, 75–102.

51 R. Iqbal, A. Matsumoto, D. Carlson, K. Peters, R. Funari, A. Sen and A. Shen, *Journal of Colloid and Interface Science*, 2022, **623**, 927–937.

52 V. Charitatos and S. Kumar, *Soft Matter*, 2020, **16**, 8284–8298.

53 V. Charitatos and S. Kumar, *Soft Matter*, 2021, **17**, 9339–9352.